Whole-genome comparisons between *Xac* and *Xcc*

We compared the genomes at the nucleotide level using the program MUMmer with default values. At the amino acid level the genomes were compared using programs developed by our bioinformatics team. Genes *g* and *h* were considered orthologues if *h* is the best BLASTP hit for *g* and vice versa, with *e*-values less than or equal to 10^{-20}. A gene was considered strain-specific if it had no hits with an *e*-value 10^{-5} or less.

Received 11 December 2001; accepted 26 March 2002.

1. Gottwald, T. R. & Graham, J. H. in *Compendium of Citrus Diseases* (eds Timmer, L. W., Garnsey, S. M. & Graham, J. H.) 5–7 (Am. Phytopathol. Soc., St. Paul, 2000).
2. Hayward, A. C. in *Xanthomonas* (eds Swings, J. G. & Civerolo, E. L.) 51–54 (Chapman & Hall, London, 1993).
3. Becker, A., Katzen, F., Puhler, A. & Ielpi, L. Xanthan gum biosynthesis and application: a biochemical/genetic perspective. *Appl. Microbiol. Biotechnol.* **50,** 145–152 (1998).
4. Menestrina, G. & Semjen, B. V. in *The Comprehensive Sourcebook of Bacterial Proteins Toxins* (ed. Alouf, J. E.) 287–309 (Academic, London, 1999).
5. Simpson, A. J. *et al.* The genome sequence of the plant pathogen *Xylella fastidiosa*. *Nature* **406,** 151–157 (2000).
6. Göttfert, M., Grob, P. & Hennecke, H. Proposed regulatory pathway encoded by the *nodV* and *nodW* genes, determinants of host specificity in *Bradyrhizobium japonicum*. *Proc. Natl Acad. Sci. USA* **87,** 2680–2684 (1990).
7. Chang, K. H. *et al.* Sequence analysis and expression of the filamentous phage phi Lf gene I encoding a 48-kDa protein associated with host cell membrane. *Biochem. Biophys. Res. Commun.* **245,** 313–318 (1998).
8. Breedveld, M. W., Hadley, J. A. & Miller, K. J. A novel cyclic β-1,2-glucan mutant of *Rhizobium meliloti*. *J. Bacteriol.* **177,** 6346–6351 (1995).
9. Ronald, P. C. & Staskawicz, B. J. The avirulence gene *avrBs1* from *Xanthomonas campestris* pv. *vesicatoria* encodes a 50-kD protein. *Mol. Plant-Microbe Interact.* **1,** 191–198 (1988).
10. Bhat, T. K., Singh, B. & Sharma, O. P. Microbial degradation of tannins—a current perspective. *Biodegradation* **9,** 343–357 (1998).
11. Beyer, S., Distler, J. & Piepersberg, W. The *str* gene cluster for the biosynthesis of 5′-hydroxy-streptomycin in *Streptomyces glaucescens* GLA.0 (ETH 22794): new operons and evidence for pathway-specific regulation by *StrR*. *Mol. Gen. Genet.* **250,** 775–784 (1996).
12. Lin, J. T., Goldman, B. S. & Stewart, V. The *nasFEDCBA* operon for nitrate and nitrite assimilation in *Klebsiella pneumoniae* M5al. *J. Bacteriol.* **176,** 2551–2559 (1994).
13. Chen, J. H., Hsieh, Y. Y., Hsiau, S. L., Lo, T. C. & Shau, C. C. Characterization of insertions of IS476 and two newly identified insertion sequences, IS1478 and IS1479, in *Xanthomonas campestris* pv. *campestris*. *J. Bacteriol.* **181,** 1220–1228 (1999).
14. Tang, J. L. *et al.* Genetic and molecular analysis of a cluster of rpf genes involved in positive regulation of synthesis of extracellular enzymes and polysaccharide in *Xanthomonas campestris* pathovar *campestris*. *Mol. Gen. Genet.* **226,** 409–417 (1991).
15. Dow, J. M., Feng, J. X., Barber, C. E., Tang, J. L. & Daniels, M. J. Novel genes involved in the regulation of pathogenicity factor production within the rpf gene cluster of *Xanthomonas campestris*. *Microbiology* **146,** 885–891 (2000).
16. Dow, J. M. & Daniels, M. J. *Xylella* genomics and bacterial pathogenicity to plants. *Yeast* **17,** 263–271 (2000).
17. Rudolf, K. in *Xanthomonas* (eds Swings, J. G. & Civerolo, E. L.) 193–264 (Chapman & Hall, London, 1993).
18. Cao, H., Baldini, R. L. & Rahme, L. G. Common mechanisms for pathogens of plants and animals. *Annu. Rev. Phytopathol.* **39,** 259–284 (2001).
19. Noël, L., Thieme, F., Nennstiel, D. & Bonas, U. cDNA-AFLP analysis unravels a genome-wide *hrpG*-regulon in the plant pathogen *Xanthomonas campestris* pv. *vesicatoria*. *Mol. Microbiol.* **41,** 1271–1281 (2001).
20. Dow, J. M., Osbourn, A. E., Wilson, T. J. & Daniels, M. J. A locus determining pathogenicity of *Xanthomonas campestris* is involved in lipopolysaccharide biosynthesis. *Mol. Plant-Microbe Interact.* **8,** 768–777 (1995).
21. Vorhölter, F. J., Niehaus, K. & Puhler, A. Lipopolysaccharide biosynthesis in *Xanthomonas campestris* pv. *campestris*: a cluster of 15 genes is involved in the biosynthesis of the LPS O-antigen and the LPS core. *Mol. Genet. Genomics.* **266,** 79–95 (2001).
22. Dums, F., Dow, J. M. & Daniels, M. J. Structural characterization of protein secretion genes of the bacterial phytopathogen *Xanthomonas campestris* pathovar *campestris*: relatedness to secretion systems of other gram-negative bacteria. *Mol. Gen. Genet.* **229,** 357–364 (1991).
23. Bonas, U. *et al.* Isolation of a gene cluster from *Xanthomonas campestris* pv *vesicatoria* that determines pathogenicity and the hypersensitive response on pepper and tomato. *Mol. Plant-Microbe Interact.* **4,** 81–88 (1991).
24. Burns, D. L. Biochemistry of type IV secretion. *Curr. Opin. Microbiol.* **2,** 25–29 (1999).
25. Wengelnik, K. & Bonas, U. HrpXv, an AraC-type regulator, activates expression of five of the six loci in the hrp cluster of *Xanthomonas campestris* pv. *vesicatoria*. *J. Bacteriol.* **178,** 3462–3469 (1996).
26. Fenselau, S. & Bonas, U. Sequence and expression analysis of the hrpB pathogenicity operon of *Xanthomonas campestris* pv. *vesicatoria* which encodes eight proteins with similarity to components of the Hrp, Ysc, Spa, and Fli secretion systems. *Mol. Plant-Microbe Interact.* **8,** 845–854 (1995).
27. Lahaye, T. & Bonas, U. Molecular secrets of bacterial type III effector proteins. *Trends Plant Sci.* **6,** 479–485 (2001).
28. Yang, Y. & Gabriel, D. W. Intragenic recombination of a single plant pathogen gene provides a mechanism for the evolution of new host specificities. *J. Bacteriol.* **177,** 4963–4968 (1995).
29. Young, N. D. The genetic architecture of resistance. *Curr. Opin. Plant Biol.* **3,** 285–290 (2000).
30. Gueneron, M., Timmers, A. C., Boucher, C. & Arlat, M. Two novel proteins, PopB, which has functional nuclear localization signals, and PopC, which has a large leucine-rich repeat domain, are secreted through the hrp-secretion apparatus of *Ralstonia solanacearum*. *Mol. Microbiol.* **36,** 261–277 (2000).

Supplementary Information accompanies the paper on *Nature*'s website (http://www.nature.com).

Acknowledgements

We thank A. M. da Silva, S. Verjovski-Almeida and D. W. Wood for reading of the manuscript; our steering committee (S. Oliver, A. Goffeau, J. Sgouros, A. C. M. Paiva and J. L. Azevedo) for their critical accompaniment; and all the technicians in the sequencing laboratories of ONSA involved in this project. Project funding was from FAPESP, Fundecitrus, Fundect-MS and CNPq.

Competing interests statement

The authors declare that they have no competing financial interests.

Correspondence and requests for materials should be addressed to A.C.R.d.S. (e-mail: acrasera@iq.usp.br). The sequences have been deposited in GenBank under accession numbers AE008922 (*Xcc* chromosome), AE008923 (*Xac* chromosome), AE008924 (pXAC33) and AE008925 (pXAC64).

The catalytic pathway of horseradish peroxidase at high resolution

Gunnar I. Berglund*†, Gunilla H. Carlsson*†, Andrew T. Smith‡, Hanna Szöke*§, Anette Henriksen§‖ & Janos Hajdu*

* *Department of Biochemistry, Uppsala University, Biomedical Center, Box 576, S-751 23 Uppsala, Sweden*
‡ *School of Biological Sciences, University of Sussex, Brighton BN1 9QG, UK*
‖ *Protein Structure Group, Department of Chemistry, University of Copenhagen, Universitetsparken 5, DK-2100 København, Denmark*
† *These authors contributed equally to this work*

A molecular description of oxygen and peroxide activation in biological systems is difficult, because electrons liberated during X-ray data collection reduce the active centres of redox enzymes catalysing these reactions[1–5]. Here we describe an effective strategy to obtain crystal structures for high-valency redox intermediates and present a three-dimensional movie of the X-ray-driven catalytic reduction of a bound dioxygen species in horseradish peroxidase (HRP). We also describe separate experiments in which high-resolution structures could be obtained for all five oxidation states of HRP, showing such structures with preserved redox states for the first time.

In 1810, Planche[6] reported that a tincture of guaiacum developed a stronger colour when a piece of fresh horseradish root was soaked in it. During the next two centuries, horseradish peroxidase (HRP), the haem-containing enzyme responsible for the colour change in Planche's experiment, was used extensively to develop ideas on redox catalysis. Haem-containing redox enzymes participate in a strikingly diverse range of chemistry, yet all biological oxidation reactions catalysed by these enzymes involve very similar high-oxidation-state intermediates (Fig. 1) whose reactivity is modulated by the protein environment[4,5,7,8]. An understanding of these enzymes in structural terms requires detailed structures for the redox intermediates. This is not a trivial task because electrons liberated in the sample by X-rays during crystallographic data collection alter the redox state of the active site[1–5]. Redox enzymes have evolved to channel electrons efficiently into an oxidized active site. Attempts to minimize radiation-induced structural changes in crystals[1,2,4,9–11] include soaking them in excess electron scavengers[12] and using short-wavelength X-rays[4]. Neither of these measures proved to be sufficient to preserve the redox state of oxidized intermediates in HRP during conventional X-ray data collection. Figure 2a and b shows that the ferric and the compound III forms of HRP became reduced by X-rays at doses smaller than those required

§ Present addresses: Lawrence Livermore National Laboratory, PO Box 808, L-41, Livermore, California 94551, USA (H.S.); Carlsberg Laboratory, Gamle Carlsberg Vej 10, DK-2100 Valby, Denmark (A.H.).

for the collection of a complete diffraction data set (wavelength range tested, 0.78–0.98 Å). These findings have implications beyond the immediate scope of this paper and raise questions about the actual oxidation state of many redox proteins in the Protein Data Bank. There is an intrinsic limit to the amount of data which can be extracted from a sample of a given size[13–15] in a given time[16–18]. Figure 2c illustrates the difficulty in obtaining a structure for the bound dioxygen species in compound III. At the start of data collection, the population of compound III was nearly 100% in the crystal (Fig. 2b). However, the electron density map in Fig. 2c gives no sign of the bound dioxygen species; instead, densities for separated water molecules appear in the active site. Electrons liberated in the sample and funnelled to the active site seem to have been used by the enzyme to cleave the bound dioxygen species. We interpret the map of Fig. 2c as a mixture of structures dominated by the products.

In order to minimize such side reactions, we employed a multi-crystal data collection strategy based on a systematic spread of the X-ray dose over many crystals (Fig. 3a). Single-crystal microspectrophotometry was then used to correlate measured structural transitions with measured electronic transitions in experiments similar to stoichiometric redox titrations. This approach permits one to drive (and control) redox reactions in crystals, using a small number of electrons redistributed in the sample crystals (for further details see Supplementary Information). Using this technique, we captured compound III (Fig. 3b top) and obtained a three-dimensional movie on the X-ray-driven catalytic conversion of the bound dioxygen species to two molecules of water in the active site (Fig. 3b). The electronic structure of compound III of HRP is similar to that of oxymyoglobin and oxyhaemoglobin and can be described as Fe^{2+}-O_2 or the isoelectronic Fe^{3+}-$O_2^{-\cdot}$ form[19]. The dioxygen bound to HRP has a significant superoxide character[20] and is highly reactive. It offers an excellent model on which the four-electron reduction of dioxygen to water can be studied in structural terms. The atomic details of this reaction have been elusive, owing to difficulties in obtaining reliable X-ray structures for oxidized redox intermediates. Figure 3b shows frames assembled from small chunks of data as shown in Fig. 3a. The results show the breakage of the oxygen–oxygen bond, the release of the first water molecule, formation of a 'ferryl-like' intermediate, and the formation of the second water molecule in agreement with the expected stoichiometry of the reaction. Electron transfer reactions and proton-coupled electron transfer processes readily occur at cryogenic temperatures in protein crystals along with small-scale movements of ligands and side chains[4,5,21–23]. The water molecule derived from the distal oxygen atom (and formed first) is within hydrogen-bonding distance of the oxygen atom remaining on the iron. This water also forms hydrogen bonds with the Nε2 atom of His 42, the side-chain of Arg 38 and another water peak (not shown here for the sake of clarity, but shown in the high-resolution structures of compounds I and II captured in separate experiments; Fig. 4d, e). At higher X-ray doses, the iron–oxygen bond breaks, leaving behind a penta-coordinated iron, which is now 0.2 Å below the plane of the pyrrole nitrogens with the iron in the ferrous state. Structural changes were limited to the active site with no measurable changes in the structures of disulphide bridges, suggesting that the active site is significantly more sensitive to reduction than the protein itself. The sequence represents changes in the average structure at the active site during exposure to X-rays. Figure 3c shows a mechanism

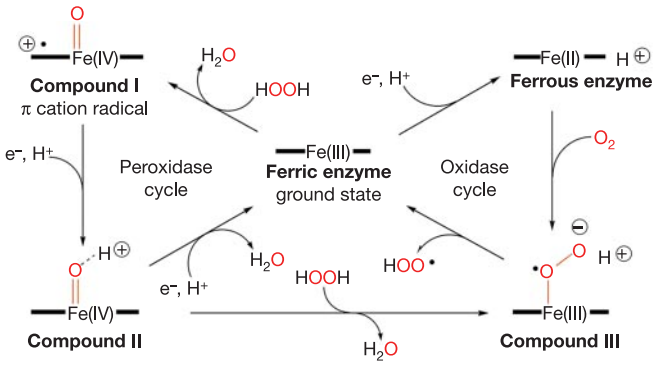

Figure 1 The five oxidation states of horseradish peroxidase.

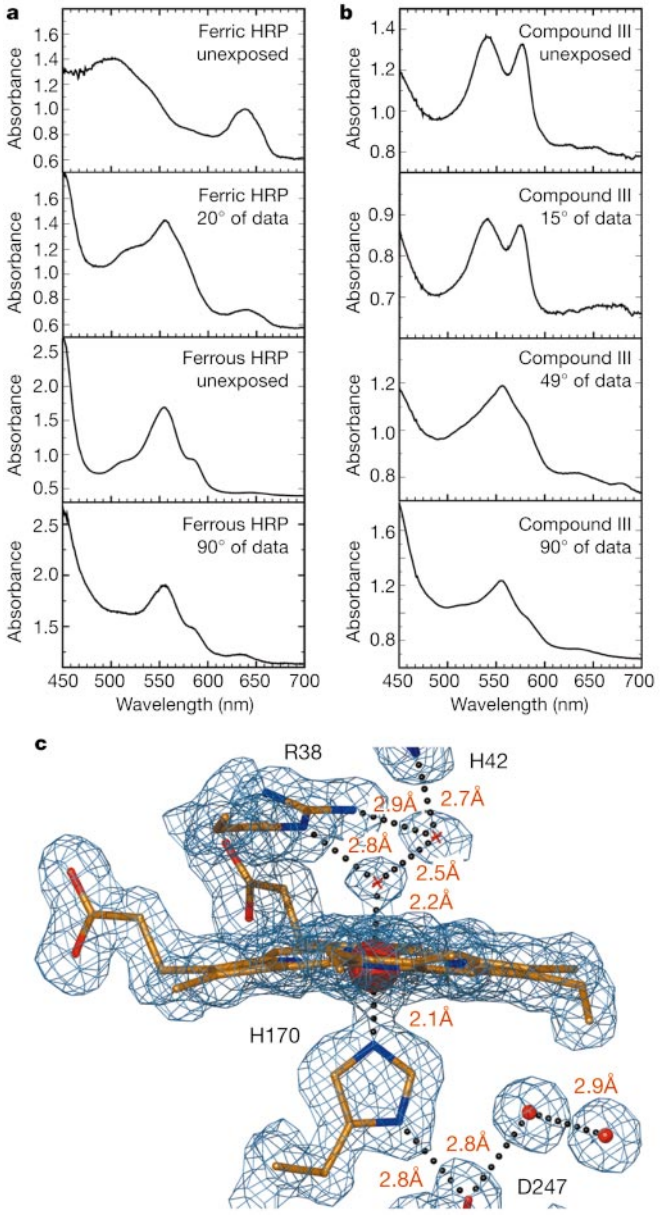

Figure 2 X-ray-induced reduction of horseradish peroxidase (wavelength range, 0.93–0.98 Å). **a**, Changes in the spectra of the ferric and ferrous forms following X-ray exposure. **b**, Spectral changes in compound III. **c**, The 1.60-Å electron-density map calculated from 90 degrees of data from a single compound III crystal. Accession code, PDB 1h5m. The density shows two solvent molecules above the iron instead of the expected dioxygen species. SigmaA-weighted[30] $2mF_{obs}$–DF_{calc} maps contoured at 1σ (σ represents the root mean square electron density for the unit cell). Carbons are coloured gold, nitrogens blue and oxygens red. This colouring scheme is used in all other figures.

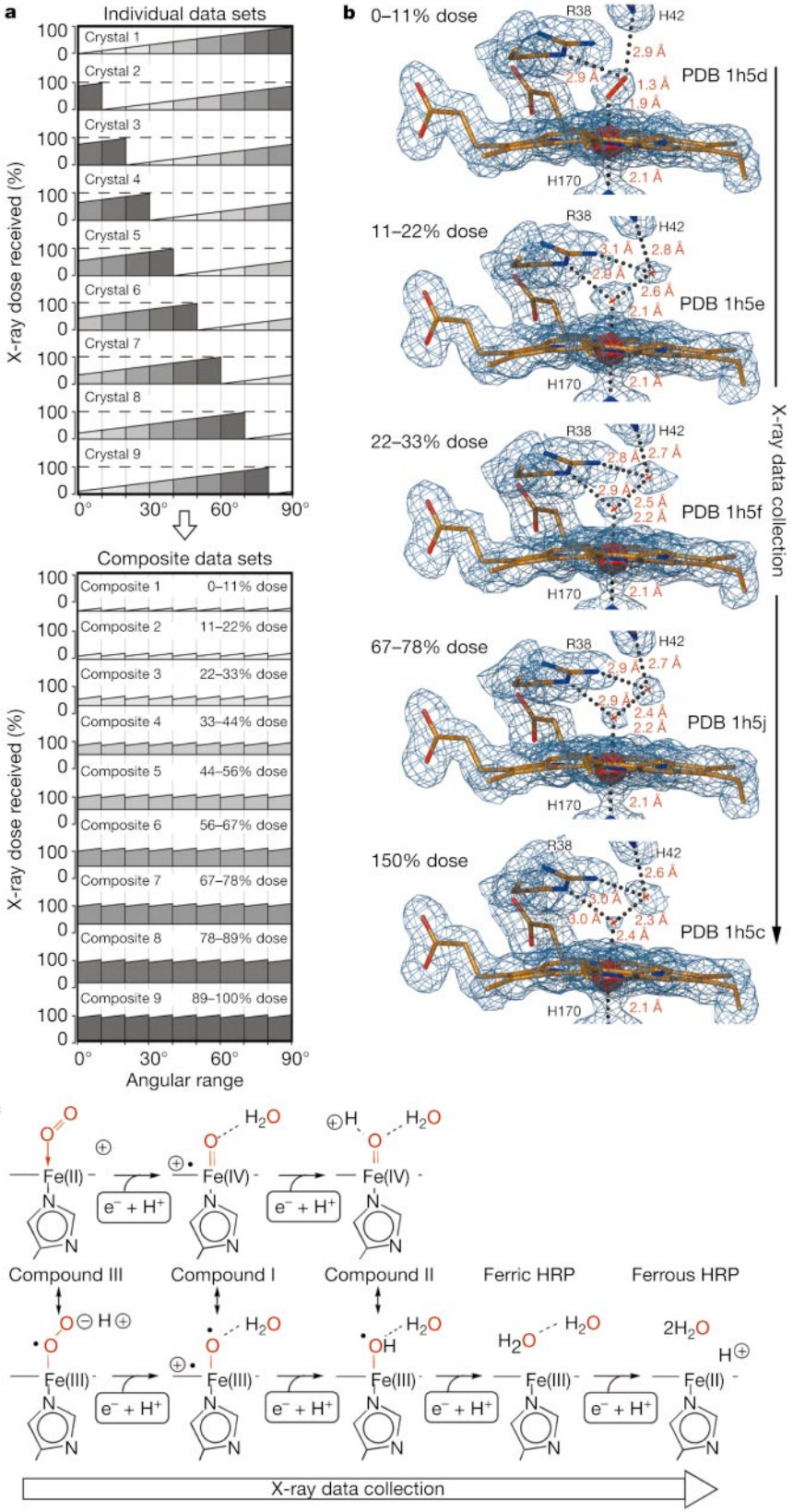

Figure 3 X-ray-driven catalytic conversion of a dioxygen species in horseradish peroxidase. **a**, The multicrystal data collection strategy, showing the distribution of the X-ray dose as a function of the rotation angle on individual (and spectrally uniform) crystals of HRP. The construction of composite data sets from small chunks of the individual data sets is shown at the bottom. Composite data sets represent structures that received different X-ray doses. This method permits experiments similar to redox titrations. **b**, SigmaA-weighted[30] $2mF_{obs}–DF_{calc}$ maps contoured at 1σ showing X-ray-induced reduction of compound III. For the last structure, the crystal was pre-exposed to X-rays for 90° before another full X-ray data set was collected on it. Accession codes are shown. **c**, A possible mechanism for the reduction of the bound dioxygen species to two molecules of water. Structures linked by double arrows are isoelectronic with each other.

which can account for the X-ray-induced transformation of the bound dioxygen species of compound III to two molecules of water in HRP.

We investigated whether this is all that happens in terms of movements during catalysis in the crystal. We performed a second set of experiments where each of the five expected intermediates was built up to high concentrations in crystals of unfrozen HRP. Each of these intermediates was then preserved for subsequent structure determination by quenching the crystals in liquid nitrogen (see Methods). Structures obtained from the first few degrees of data for these intermediates are shown in Fig. 4 and the crystallographic data are summarized in the Supplementary Information.

Figure 4a shows the structure of the pure ferric form. The ferric iron is penta-coordinated and is predominantly high-spin[7,8]. Density for an acetate ion (from the crystallization solution, see Methods) is visible above the haem plane. In the structure of the acetate-free form of the enzyme[24], two solvent molecules take up the oxygen positions of the acetate. Acetate can be washed away from the crystal and is not present in the structures of intermediates (Fig. 4b–e).

Figure 4b shows the structure of the pure ferrous form. This structure was obtained by soaking ferric crystals in dithionite before freezing the crystal in liquid nitrogen. The enzyme remained in the reduced, ferrous state during data collection, and a full data set

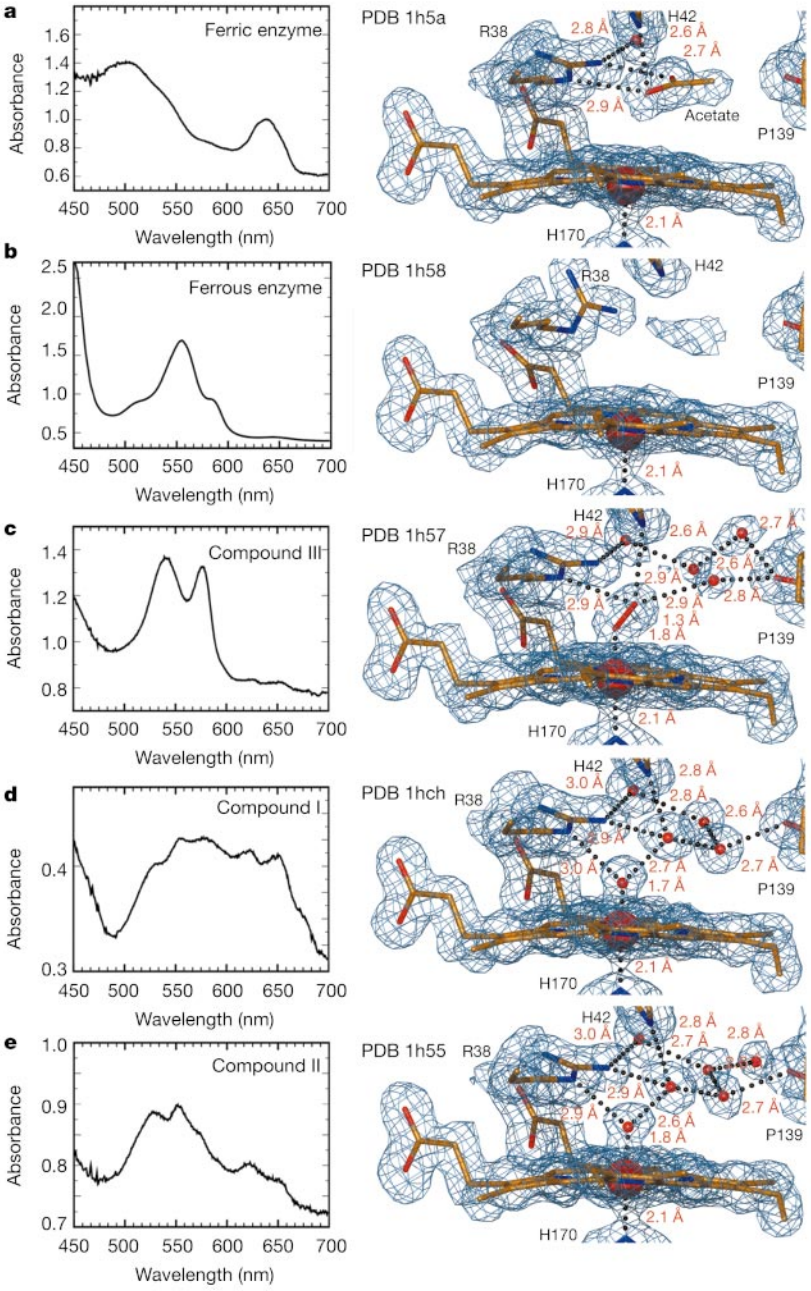

Figure 4 Spectra and refined high-resolution structures for the five oxidation states of horseradish peroxidase. Accession codes are shown. The structures were captured at high concentrations in individual experiments (Methods) and were obtained from the first few degrees of data (Table 2 of the Supplementary Information). **a**, Ferric enzyme. **b**, Ferrous enzyme. **c**, Compound III (Fe–O bond distance, 1.8 Å). **d**, Compound I (Fe–O bond distance, 1.7 Å). **e**, Compound II (Fe–O bond distance, 1.8 Å). SigmaA-weighted[30] $2mF_{obs}–DF_{calc}$ maps contoured at 1σ.

could be collected on one crystal (Fig. 2a, bottom).

Figure 4d shows the structure of an 80% pure compound I in which one electron is withdrawn from the ferric iron and a second from the porphyrin ring to give an oxoferryl species and a porphyrin π-cationic radical. Compound I was produced by reacting ferric HRP crystals with peracetic acid. Peracetic acid can oxidize HRP to compound I, but cannot react with it further; thus a practically complete conversion of the crystal to compound I can be achieved. In order to suppress unwanted side reactions, we used crystals grown from trans-3-methoxycinnamic acid, a compound which is not susceptible to oxidation by the enzyme. At the beginning of data collection, the visible absorption spectrum of the crystals suggested nearly pure compound I. Compound I is, however, extremely labile and about a third of it was converted to compound II already after the collection of 8° of data at 0.78 Å wavelength. The structure calculated from composite data obtained from 11 crystals (Fig. 4d) is predominantly compound I (80%), but it also contains about 20% compound II on average, as judged by the spectral data. The iron–oxygen bond distance in this structure is 1.7 Å, which agrees well with extended X-ray absorption fine structure (EXAFS) measurements (1.64 Å)[25]. Electron-density maps calculated with the program EDEN[26] (Methods) confirm our interpretation of the data. The refined structure indicates an occupancy of at least 85% for the bound oxygen atom on the iron. This value is based on the assumption that the *B*-factor of the covalently attached oxygen atom was not significantly different from *B*-factors in its immediate vicinity. The ferryl oxygen forms hydrogen bonds with the Nε atom of Arg 38 (3.0 Å) and with a water molecule (2.7 Å). This water is hydrogen-bonded to His 42 (2.8 Å) and Arg 38 (2.9 Å, Fig. 4d) and occupies the position of the first-formed water in Fig. 3.

Figure 4e shows the structure of compound II. Spectral data show that this species was at least 80% pure. The ferryl oxygen of compound II has an occupancy close to 100%. There is no direct hydrogen bond between His 42 and the ferryl oxygen in compounds I or II. The ferryl oxygen of compound II makes hydrogen bonds to the Nε atom of Arg 38 (2.9 Å) and to a water molecule (2.6 Å) hydrogen-bonded to His 42 (2.8 Å) and Arg 38 (2.9 Å, Fig. 4e). The active site of HRP stabilizes a net positive charge on the haem in compound I, but in compound II this π-cationic radical is no longer present. The electron densities in Fig. 4d and e show a hydrogen bond between the ferryl oxygen and the density at the position of the first-formed water molecule in Fig. 3. This interaction is very similar in compounds I and II. In compound II, however, a proton is believed to have moved to the ferryl oxygen, probably from His 42 via the intervening water-molecule, priming the formation of the second product water in the reaction. The iron–oxygen bond is 0.14 Å longer in compound II than in compound I, giving an iron–oxygen distance of 1.8 Å (1.93 Å by EXAFS[25]). The longer Fe–O bond supports the argument for the migration of a proton to the ferryl oxygen, following the removal of the π-cationic radical in compound II.

Figure 4c shows the structure of a 95% pure compound III. The refined occupancy of the dioxygen species was about 95%. The dioxygen species ligates the haem iron in a bent conformation with the OA atom 1.8 Å away from the iron (1.72 Å by EXAFS[25]). The Fe–OA–OB angle is 126°. The OB atom forms hydrogen bonds with the Nε2 atom of His 42 (2.9 Å), the Nε atom of Arg 38 (2.9 Å) and with a water molecule (2.9 Å). His 42 moves 0.5 Å towards the distal oxygen atom of the bound dioxygen species. Arg 38 moves 0.2 Å towards this oxygen and forms a hydrogen bond. The haem iron together with His 170 moves 0.2 Å towards the plane of the pyrrole nitrogens as a result of dioxygen binding.

All structural results show changes specific to the active site. There are four disulphide bridges in HRP and they remained unperturbed during data collection on compounds I, II, III and on the ferric enzyme. The Cys 97–Cys 301 disulphide bridge is partially broken in the ferrous enzyme, probably as a result of reduction with dithionite. Cys 11–Cys 91 can be modelled in two conformations in all structures, which suggests genuine disorder in this area in HRP.

Charge-exchange reactions between highly oxidized metal centres and neutral molecules are important in difficult synthetic and degradative processes in chemistry and biology and have recently been identified as the source of cometary X-ray emission[27]. After dioxygen began to be produced by photosynthetic organisms on Earth, the maximum oxidation/ionization states attainable by metal centres in biocatalysis rose swiftly. The catalytic intermediates of HRP described in this paper show these structures with preserved redox state for what we believe is the first time. We suggest that similar structures exist in cytochromes P450 and the terminal oxidases of aerobic respiratory chains. The results presented here provide direct structural insights into the redox chemistry behind these processes at porphyrin-based iron centres. □

Methods

Crystallization of ferric HRP

Crystals[28] of recombinant HRP[29] were grown from 20% polyethylene glycol (PEG) 8000, 0.2 M calcium acetate, 0.1 M sodium cacodylate, pH 6.5 by vapour diffusion at 4 °C, using streak seeding. Two crystallizations were set up: (1) For studies on the ferric, ferrous, compound II and compound III forms, the droplets contained 2 μl protein (7.3 mg ml^{-1} in 0.1 M cacodylate, pH 6.5), 2 μl reservoir solution and 1 μl isopropanol saturated with ferulic acid. Before the experiments, crystals were washed twice overnight in 5 μM hydrogen peroxide in reservoir solution to remove bound ferulic acid. (2) For studies on compound I, crystals were grown in droplets containing 3 ml protein (7.3 mg ml^{-1}), 3 μl reservoir solution and 0.5 μl isopropanol saturated with trans-3-methoxycinnamic acid. Trans-3-methoxycinnamic acid was removed by washing these crystals in reservoir solution twice overnight. Absorption spectra showed that both types of washed crystals were in the ferric state. Consequent reactions in non-frozen crystals were all performed at 4 °C.

Preparation of ferrous crystals

The ferrous state was formed by soaking ferric crystals for 30 min in a reservoir solution supplemented with 100 mM sodium dithionite and 10% PEG 400.

Preparation of compound III in crystals

Compound III developed within 2–5 min after placing ferric HRP crystals in 54 mM hydrogen peroxide, 10 μM ferulic acid, and 10% PEG 400.

Preparation of compound I in crystals

Compound I was produced by soaking washed crystals in a droplet of 1–2 mM peracetic acid dissolved in reservoir solution. Compound I has a greenish colour that developed in 2–10 min. Crystals were flash frozen in liquid nitrogen, following exposure to 10% PEG 400 in reservoir solution for cryoprotection.

Preparation of compound II in crystals

Compound II was produced in washed crystals following a soak in a droplet of 2–5 mM peracetic acid dissolved in reservoir solution, which also contained 10% PEG 400. After the green colour of compound I had disappeared (2–20 min), the crystals were flash frozen.

Flash freezing and single crystal microspectrophotometry

All crystals were flash frozen in liquid nitrogen and stored for data collection. Their spectra were measured at 100 K before and after X-ray exposure with a microspectrophotometer (4DXray Systems AB; http://www.4dx.se) linked to an Oxford CryoStream cooler (OxfordCryosystems; http://www.oxfordcryosystems.co.uk). Wherever possible, care was taken to record spectra in similar crystal orientations. Spectral deconvolution was performed with SigmaPlot 3.0 (Jandel Scientific). Spectra of frozen crystals remained unchanged during storage.

X-ray data collection and processing

Data were collected at 100 K at BM14 and ID14 EH3 of the ESRF (Grenoble, France) and at I-711 at MaxLab (Lund, Sweden) with X-rays of the shortest possible wavelengths. Crystals of HRP were aligned to allow collection of a complete data set with 90 degrees rotation. The strategies outlined in Fig. 3a were applied. Data were processed and scaled using the HKL package (http://www.hkl-xray.com) and programs in the CCP4 suite (http://www.ccp4.ac.uk).

Crystallographic refinement

Starting coordinates (7atj; ref. 28) included the protein moiety and the haem group. Identical test sets (with reflections of the same indices) were used to calculate and compare R_{free} values for the different structures. Models were refined with an amplitude-based maximum-likelihood target in the program CNS (http://cns.csb.yale.edu) applying overall *B*-factor corrections and bulk solvent corrections. In the final stages of the refinements, the iron, the porphyrin and any ligand bound to the distal side of the haem iron were refined as

separate non-bonded groups using only X-ray terms in the target function. SigmaA-weighted electron-density maps[30] and the program EDEN[26] were used to check and to eliminate model bias. In the EDEN runs, the haem and its ligands were removed from the protein model and EDEN was used with a gentle solvent target to recover these missing molecules completely. In all cases shown here, the haem and its bound ligands were recovered and the electron density was at least as clear as in the starting maps, indicating that refinement proceeded without model bias. In order to perform further tests, the EDEN solution was perturbed by independently changing amplitudes and phases in the file of the calculated structure factor amplitudes (F_{calc}), using a 30% random gaussian perturbation; the resulting perturbed F_{calc} file served as the starting model for another EDEN run. The perturbation/recovery steps were repeated 10 times and the resulting 10 maps were then averaged. These maps showed excellent agreements with the starting maps. Occupancy of the ligands were refined in SHELXL (http://shelx.uni-ac.gwdg.de/SHELX).

Models were inspected with O (http://xray.bmc.uu.se/alwyn) and figures were rendered by POV-Ray (http://www.povray.org), using the Molray interface at http://xray.bmc.uu.se/markh.

Coordinates and structure factors have been deposited in the Protein Data Bank (accession codes 1h5m, 1h5d, 1h5e, 1h5f, 1h5g, 1h5h, 1h5i, 1h5j, 1h5k, 1h5l, for the structures in Table 1 of the Supplementary Information and 1h58, 1h5a, 1h57, 1h5c, 1hch and 1h55 for the structures in Table 2 of the Supplementary Information).

Received 11 November 2001; accepted 4 March 2002.

1. Chance, B., Angiolillo, P., Yang, E. K. & Powers, L. Identification and assay of synchrotron radiation-induced alterations on metalloenzymes and proteins. *FEBS Lett.* **112,** 178–182 (1980).
2. Logan, D. T. *et al.* Crystal structure of reduced protein R2 of ribonucleotide reductase: the structural basis for oxygen activation at a dinuclear iron site. *Structure.* **4,** 1053–1064 (1996).
3. Harrenga, A. & Michel, H. The cytochrome c oxidase from *Paracoccus denitrificans* does not change the metal center ligation upon reduction. *J. Biol. Chem.* **274,** 33296–33299 (1999).
4. Schlichting, I. *et al.* The catalytic pathway of cytochrome p450cam at atomic resolution. *Science* **287,** 1615–1622 (2000).
5. Sjögren, T. & Hajdu, J. Structure of the bound dioxygen species in the cytochrome oxidase reaction of cytochrome cd1 nitrite reductase. *J. Biol. Chem.* **276,** 13072–13076 (2001).
6. Planche, L. A. Note sur la sophistication de la résine de jalap et sur les moyens de la reconnaître. *Bull. Pharmacie* **2,** 578–580 (1810).
7. Dunford, H. B. *Heme Peroxidases* (Wiley, New York, 1999).
8. Veitch, N. C. & Smith, A. T. *Advances in Inorganic Chemistry* Vol. 51**,** 107–162 (Academic, New York, 2001).
9. Weik, M. *et al.* Specific chemical and structural damage to proteins produced by synchrotron radiation. *Proc. Natl Acad. Sci. USA* **97,** 623–628 (2000).
10. Burmeister, W. P. Structural changes in a cryo-cooled protein crystal owing to radiation damage. *Acta Crystallogr. D* **56,** 328–341 (2000).
11. Leiros, H.-K. S., McSweeney, S. M. & Smalås, A. O. Atomic resolution structures of trypsin provide insight into structural radiation damage. *Acta Crystallogr. D* **57,** 488–497 (2001).
12. Lancaster, C. R., Kroger, A., Auer, M. & Michel, H. Structure of fumarate reductase from *Wolinella succinogenes* at 2.2 Å resolution. *Nature* **402,** 377–385 (1999).
13. Henderson, R. Cryoprotection of protein crystals against radiation-damage in electron and X-ray diffraction. *Proc. R. Soc. Lond. B,* **241,** 6–8 (1990).
14. Henderson, R. The potential and limitations of neutrons, electrons and X-rays for atomic resolution microscopy of unstained biological molecules. *Q. Rev. Biophys.* **28,** 171–193 (1995).
15. Gonzales, A. & Nave, C. Radiation damage in protein crystals at low temperature. *Acta Crystallogr. D* **50,** 874–877 (1994).
16. Neutze, R., Wouts, R., van der Spoel, D., Weckert, E. & Hajdu, J. Potential for biomolecular imaging with femtosecond X-ray pulses. *Nature* **406,** 752–757 (2000).
17. Ziaja, B., van der Spoel, D., Szöke, A. & Hajdu, J. Auger-electron cascades in diamond and amorphous carbon. *Phys. Rev. B* **64,** 214104-1–214104-8 (2001).
18. Persson, P., Lunell, S., Szöke, A., Ziaja, B. & Hajdu, J. Shake-up and shake-off excitations with associated electron losses in X-ray studies of proteins. *Protein Sci.* **10,** 2480–2484 (2001).
19. Nakajima, R. & Yamazaki, I. The mechanism of oxyperoxidase formation from ferryl peroxidase and hydrogen peroxide. *J. Biol. Chem.* **262,** 2576–2581 (1987).
20. Van Wart, H. E. & Zimmer, J. Resonance Raman evidence for the activation of dioxygen in horseradish oxyperoxidase. *J. Biol. Chem.* **260,** 8372–8377 (1985).
21. Hammes-Schiffer, S. Theoretical perspectives on proton-coupled electron transfer reactions. *Acc. Chem. Res.* **34,** 273–281 (2001).
22. Schlichting, I., Berendzen, J., Phillips, G. N. Jr & Sweet, R. M. Crystal structure of photolysed carbonmonoxy-myoglobin. *Nature* **371,** 808–812 (1994).
23. Edman, K. *et al.* High-resolution X-ray structure of an early intermediate in the bacteriorhodopsin photocycle. *Nature* **401,** 822–826 (1999).
24. Gajhede, M. *et al.* Crystal structure of horseradish peroxidase C at 2.15 angstrom resolution. *Nature Struct. Biol.* **4,** 1032–1038 (1997).
25. Chance, B. *et al.* X-ray absorption studies of intermediates in peroxidase activity. *Arch. Biochem. Biophys.* **235,** 596–611 (1984).
26. Szöke, A. Use of statistical information in X-ray crystallography with application to the holographic method. *Acta Crystallogr. A* **54,** 543–562 (2001).
27. Cravens, T. E. Comet Hyakutake X-ray source: Charge transfer of solar wind heavy ions. *Geophys. Res. Lett.* **24,** 105–108 (1997).
28. Henriksen, A., Smith, A. T. & Gajhede, M. The structures of the horseradish peroxidase C-ferulic acid complex and the ternary complex with cyanide suggest how peroxidases oxidize small phenolic substrates. *J. Biol. Chem.* **274,** 35005–35011 (1999).
29. Smith, A. T. *et al.* Expression of a synthetic gene for horseradish peroxidase C in *Escherichia coli* and folding and activation of the recombinant enzyme with calcium and heme. *J. Biol. Chem.* **265,** 13335–13343 (1990).
30. Read, R. J. Improved Fourier coefficients for maps using phases from partial structures with errors. *Acta Crystallogr. A* **42,** 140–149 (1986).

Supplementary Information accompanies this paper on *Nature*'s website (http://www.nature.com).

Acknowledgements

We thank M. Gajhede, K. G. Welinder, N. Veitch, B. Ziaja, D. Choudhury, M. Iwata, R. Subramanian and G. Katona for discussions and help. We thank MaxLab and ESRF/EMBO for beam time and services. This work was supported by the EU-Biotech Programme and by the Swedish Research Councils.

Competing interests statement

The authors declare that they have no competing financial interests.

Correspondence and requests for materials should be addressed to J.H. (e-mail: janos@xray.bmc.uu.se).

retraction

Directed evolution of new catalytic activity using the α/β-barrel scaffold

M. M. Altamirano, J. M. Blackburn, C. Aguayo & A. R. Fersht

Nature **403**, 617–622 (2000).

This laboratory reported the *in vitro* evolution of an enzyme with phosphoribosyl anthranilate isomerase activity (ivePRAI) from the α/β-barrel scaffold of indole-3-glycerol-phosphate synthase using a combination of rationally designed libraries, DNA shuffling, and selection with *Escherichia coli*, JA300, a strain that lacks an active PRAI gene. As part of the ongoing project to characterize the structure and properties of ivePRAI, we discovered that the protein expressed from a variety of vectors that contained a synthetic gene corresponding to the sequence of ivePRAI as published is insoluble and does not complement JA300 (R. L. Weinberg, C. M. Blair and A.R.F., unpublished results), as reported. We conclude that the results are unsound.

It appears that the discrepancy in the results is due to a combination of two episodes of cross-contamination. We are now repeating the directed evolution of ivePRAI using modified procedures to test the design strategy that should eliminate the source of errors of contamination.

The first author of this Article (M.M.A.), who was responsible for most of the analysis and design strategy involving loop transfer and most of the experimental work, wishes to be dissociated from this retraction because she believes that the experimental data are fundamentally sound. □